Proceedings of ASME Turbo Expo 2011
GT2011
June 6-10, 2011, Vancouver, British Columbia, Canada

GT2011-45806

ANALYSIS OF UNSTEADINESS ON CASING TREATMENT MECHANISMS IN AN AXIAL COMPRESSOR

G. Legras
SNECMA-SAFRAN GROUP
Aerodynamics Methods
and Tools Development Department
Rond Point René Ravaud
77550, Moissy-Cramayel, France
Email: legras@cerfacs.fr

N. Gourdain
CERFACS
Computational Fluid Dynamics Team
42 av. Gaspard Coriolis
31057, Toulouse, France
Email: gourdain@cerfacs.fr

I. Trébinjac
X. Ottavy
LMFA, UMR 5509
Ecole Centrale de Lyon / UCBLyon I / INSA
69134, Ecully; France
Email: isabelle.trebinjac@ec-lyon.fr
xavier.ottavy@ec-lyon.fr

ABSTRACT

Control devices based on casing treatments have already shown their capability to improve the flow stability in compressors. However their optimization remains complex due to a partial understanding of the related physical mechanisms. The present paper proposes to use a budget analysis of the Navier Stokes equations to support the understanding of such flow phenomena. Based on the original work of Shabbir and Adamczyk (2005), the strength of the present contribution is to generalize the flow analysis method to all Navier-Stokes equations, including unsteady terms. A high-pressure multistage compressor equipped with circumferential casing grooves is chosen to demonstrate the potential of this approach. Steady and unsteady Reynolds-Averaged Navier-Stokes (URANS) equations are solved with a structured multi-blocks solver. Results are then briefly compared to experimental data to validate the numerical method. The analysis of the unsteady axial momentum equation for configurations with and without casing treatment points out some of the mechanisms responsible for the stability improvement. The analysis also indicates that the flow unsteadiness generated by upstream stator wakes (stator/rotor interaction) reduces viscous efforts and increases convective forces, significantly modifying the compressor stability. Finally, the proposed post processing method shows very interesting results for the understanding of circumferential grooves and it should be also used for non-axisymmetric casing treatment configurations.

NOMENCLATURE

Symbols

$\mathbf{A}$	surface area of a grid cell, $= [A_r, A_\theta, A_z]^T$
E_r	relative energy
F_{cen}	centrifugal force
F_{cor}	Coriolis force
$F_{\lambda_{2,4}}$	2^{nd} and 4^{th} order numerical scalar artificial dissipation fluxes
h	distance from the hub
H	height of the vein
$\dot{m}$	mass flow rate
P_s	static pressure
Pt	total pressure
$\mathbf{q}$	heat flux vector, $= [q_r, q_\theta, q_z]^T$
Q	conservative variable
$\mathbf{R}$	numerical modelling residual
R	number of rotor row
Rpi	total-to-total pressure ratio
r, θ, z	cylindrical coordinates
S	number of stator row
t	time
$T_{R,S}$	rotor/stator blade passing temporal period
V	volume of the control domain
$\mathbf{V}$	absolute velocity, $= [V_r, V_\theta, V_z]^T$
$\mathbf{W}$	relative velocity, $= [W_r, W_\theta, W_z]^T$

Greek letters

η_{is}	isentropic efficiency
γ	specific heat ratio
μ	molecular dynamic viscosity
ω	rotation speed
ρ	density
τ	sum of the viscous and turbulence stress tensor

Acronyms

CT	Casing Treatment
ESA	Extended Shabbir and Adamczyk model
LDA	Laser Doppler Anemometer
SW	Smooth Wall

INTRODUCTION

Today, it is mandatory for compressor designers to improve performance in terms of efficiency and operating range characterized by the stall margin at low mass flow rate. One of the main difficulties encountered in this process is that compressor stall is not always controlled through normal aerodynamic design. Thus stall prevention techniques must be used and one promising technology known to bring substantial stability in the rotor tip region is Casing Treatment (CT) (Greitzer et al. [1]). This kind of technology consists of slots or grooves within the rotor casing. Hathaway [2] provides an extensive overview of the research studies over the last 50 years that attempt to uncover the physics behind the improvement in stall margin. Among many of the geometries that have been experimentaly and numerically investigated are circumferential casing grooves (Rabe et al. [3], Shabbir and Adamczyk [4], Perrot et al. [5], Müller et al. [6, 7], Houghton and Day [8], Legras et al. [9, 10]), non-axisymmetric slot-type CT (Wilke et al. [11, 12], Gourdain and Lebœuf [13], Vogues et al. [14], Schnell and al. [15]) and self-recirculating flow channels (Hathaway [16], Yang et al. [17], Strazisar et al. [18]).

However, this understanding is not complete since experimental measurements in the near casing region are still very rare. Moreover, simple analysis using 2D or 3D flow fields hardly allows a quantification and can cause in some cases a mis-understanding of the flow mechanisms. Therefore, CT design requires analysis methods that need to be as easy as possible to handle for aeroengine designers. In this context, Shabbir and Adamczyk [4] proposed an approach based on a budget analysis of the steady axial momentum equation close to the rotor casing. This methodology provides further insight into the flow mechanisms relevant to compressor stability systems. In fact, their paper shows that the approach is useful to ascertain that CT improves the flow stability and it provides guidance for grooves design (especially regarding the optimal number of grooves). However, Shabbir and Adamczyk [4] methodology is restrained to the knowledge of changes in the balance of steady axial momentum equation while CT interaction with the main flow is strongly complex, thus requiring information coming from each of the Navier-Stokes equation.

In order to further understand and quantitatively diagnose complex flow mechanisms induced by any CT, the current paper presents a generalization of the methodology originally proposed by Shabbir and Adamczyk [4]. This novel model calculates the budget analysis of the Navier-Stokes set of unsteady equations. It has been successfully applied by Legras et al. [10] to investigate the flow mechanisms induced by circumferential CT on the NASA Rotor 37 using the budget of the steady axial and radial momentum equations. In order to apprehend this novel method for unsteady problem, the present paper analyses the influence of upstream stator wakes on groove mechanisms in a subsonic multistage compressor incorporating a circumferential CT. Numerical data are obtained with unsteady flow simulations. Smooth wall (SW) configuration and CT case are compared. LDA measurements in the immediate vicinity of the CT are used for comparison and validation of the unsteady numerical simulations. Afterwards, the Extended Shabbir and Adamczyk (ESA) model is used to evaluate the budget analysis of the unsteady axial momentum equation at the rotor tip region based on the numerical results.

Finally, it is worth noticing that the ESA method could be easily taken for uncovering flow mechanisms and for designing a large panel of flow passive control devices: film cooling, boundary layer aspiration in turbomachinery field as well as in aircraft or helicopter domain.

FLOW ANALYSIS METHODOLOGY

Equations

A control volume fixed in time and located in the near casing flow is retained. This will provide a quantitative understanding of the relevant fluid mechanisms associated with SW and CT configurations. Thus, the balance between the various terms which appears in the Navier-Stokes equations is analyzed based on its finite volume formulation. For simplicity reasons, the equations are considered in the relative rotor frame and in cylindrical coordinates. Using the divergence theorem, the Navier-Stokes equations in integral form can be written as follows:

$$V \int_{\partial t} \frac{\partial \mathbf{Q}}{\partial t} = - \oint_{\partial \Omega} \left[\mathbf{B}\, dA_r + \mathbf{C}\, dA_\theta + \mathbf{D}\, dA_z \right] + V\, \mathbf{T} \qquad (1)$$

where A_r, A_θ and A_z are the projection areas of the control volume, V the constant volume of the control domain, $\mathbf{Q}$ the conservative variables, $\mathbf{B}$, $\mathbf{C}$ and $\mathbf{D}$ vectors resulting from the development of the advective and diffusive fluxes and $\mathbf{T}$ the forces per unit volume (usually named source terms). These vectors are recalled in Eqn. 2. The stresses in Eqn. 2 include both viscous and Reynolds stresses. In the same manner, the heat flux takes into

account the heat flux and the enthalpy turbulent diffusion flux. This last term and the Reynolds stresses are both approximated by an eddy viscosity model.

$$\mathbf{Q}=\begin{bmatrix}\rho\\ \rho W_r\\ \rho W_\theta\\ \rho W_z\\ \rho E_r\end{bmatrix}\quad \mathbf{B}=\begin{bmatrix}\rho W_r\\ \left(\rho {W_r}^2+P_s\right)-\tau_{rr}\\ \rho W_\theta W_r-\tau_{\theta r}\\ \rho W_z W_r-\tau_{zr}\\ \left(\rho E_r+P_s-\tau_{rr}\right)W_r-\left(W_\theta\tau_{r\theta}+W_z\tau_{rz}+q_r\right)\end{bmatrix}$$

$$\mathbf{C}=\begin{bmatrix}\rho W_\theta\\ \rho W_r W_\theta-\tau_{r\theta}\\ \left(\rho {W_\theta}^2+P_s\right)-\tau_{\theta\theta}\\ \rho W_z W_\theta-\tau_{z\theta}\\ \left(\rho E_r+P_s-\tau_{\theta\theta}\right)W_\theta-\left(W_r\tau_{\theta r}+W_z\tau_{\theta z}+q_\theta\right)\end{bmatrix}$$

$$\mathbf{D}=\begin{bmatrix}\rho W_z\\ \rho W_r W_z-\tau_{rz}\\ \rho W_\theta W_z-\tau_{\theta z}\\ \left(\rho {W_{zz}}^2+P_s\right)-\tau_{zz}\\ \left(\rho E_r+P_s-\tau_{zz}\right)W_z-\left(W_r\tau_{zr}+W_\theta\tau_{z\theta}+q_z\right)\end{bmatrix}$$

$$\mathbf{T}=\begin{bmatrix}0\\ \dfrac{\rho {W_\theta}^2-P_s-\tau_{\theta\theta}}{r}+2\rho\omega W_\theta+\rho\omega^2 r\\ \dfrac{\rho W_\theta W_r-\tau_{r\theta}}{r}-2\rho\omega W_r\\ 0\\ \rho\omega^2 r W_\theta\end{bmatrix} \tag{2}$$

Numerical Resolution

Since the objective is to understand the balance of the various terms using numerical CFD results, the semi-discretised in space for un-coupled time/space integration formulation of the Eqn. 1 is considered. For an individual basic hexahedral cell, this formulation is written as follows:

$$\frac{\partial\mathbf{Q}}{\partial t}=-\frac{1}{V}\left[\sum_{l=1}^{6}\mathbf{F}\cdot\mathbf{N}_{\Sigma_l}-V\,\mathbf{T}\right]=-\frac{1}{V}\mathbf{R}\left(\mathbf{Q}\right) \tag{3}$$

where l designates the l^{th} face bounding the cell, $\mathbf{F}$ the numerical approximation of the exact flux (including the below tensors $\mathbf{B}$, $\mathbf{C}$ and $\mathbf{D}$), $\mathbf{N}_{\Sigma_l}$ the external (non unit) normal to the face $\Sigma_l=[A_{rl},A_{\theta l},A_{zl}]^T$ and $\mathbf{R}$ the numerical modelling residual of variable $\mathbf{Q}$.

In order to access the information of all individual terms, a computation post-processing tool has been developped. Since the volume does not depend on time, the source terms $\mathbf{T}$ can be directly determinated using Eqn. 2. Concerning the time derivative terms, the choice is done to determine those terms at instant n by computing the opposite of the numerical modelling residual at the same instant:

$$V\,\frac{\partial\mathbf{Q}_n}{\partial t}=-\mathbf{R}\left(\mathbf{Q}_n\right) \tag{4}$$

Therefore, only the convective fluxes have to be computed (here with a 2$^{\text{nd}}$-order centered Jameson scheme (Jameson et al. [19]).

Since most CFD codes solve the Navier-Stokes equations in the cartesian reference frame, a specific treatment was done to recover terms of Eqn. 2 in cylindrical coordinates. To do so, the fluxes constitutive of terms in Eqn. 2 are build up through projection of the cartesian fluxes into the cylindrical reference frame. This strategy, instead of applying a cylindrical spatial scheme, permits to ensure the same numerical modelling residual than in the cartesian equations. Equation 5 presents the transformation matrix P for rotation by an angle of θ over the longitudinal direction (i.e. z). Equation 6 recalls the expressions for projections from cartesian to cylindrical coordinates of the face areas $\mathbf{A}$, the relative velocity vector $\mathbf{W}$, the stress tensor τ and the heat flux vector $\mathbf{q}$.

$$P=\begin{bmatrix}\cos\theta & -\sin\theta & 0\\ \sin\theta & \cos\theta & 0\\ 0 & 0 & 1\end{bmatrix} \tag{5}$$

$$\begin{aligned}\mathbf{A}_{r\theta z}&=P^{-T}\cdot\mathbf{A}_{xyz} & \mathbf{W}_{r\theta z}&=P^{-T}\cdot\mathbf{W}_{xyz}\\ \tau_{r\theta z}&=P^{-T}\cdot\tau_{xyz}\cdot P & \mathbf{q}_{r\theta z}&=P^{-T}\cdot\mathbf{q}_{xyz}\end{aligned} \tag{6}$$

For sake of clarity, the nomenclature used by Shabbir and Adamczyk [4] is chosen. The operator $\triangle()=\sum_{l=1}^{6}()$ is introduced and characterizes the balance of flux on an individual basic cell. For example, the term $\triangle(\rho W_z W_r A_r)$ appearing in the axial momentum equation corresponds to the transport of the axial momentum across the radial faces of a basic grid cell.

The objective is to understand the balance of the various terms by using data on a mesh grid. Thus, it is obvious that the control volume retained is based on this mesh. In consequence, the current approach is extended to a control volume composed of multiple grid cells. The operator $\sum_r\sum_\theta\sum_z()=\sum_{r,\theta,z}()$ is introduced and realizes the cumulative sum on each individual grid cell. For example, the unsteady axial momentum equation can be written as follows:

$$\begin{aligned}&\sum_{r,\theta,z}\triangle(\rho W_z W_r A_r)+\sum_{r,\theta,z}\triangle(\rho W_z W_\theta A_\theta)+\sum_{r,\theta,z}\triangle(\rho {W_z}^2 A_z)+\sum_{r,\theta,z}\triangle(P_s A_z)\\ &+\sum_{r,\theta,z}(F_{\lambda_2})+\sum_{r,\theta,z}(F_{\lambda_4})-\sum_{r,\theta,z}\triangle(\tau_{rz}A_r)-\sum_{r,\theta,z}\triangle(\tau_{\theta z}A_\theta)-\sum_{r,\theta,z}\triangle(\tau_{zz}A_z)\\ &=R(\rho W_z)=V\frac{\partial\rho W_z}{\partial t}\end{aligned} \tag{7}$$

where F_{λ_2} and F_{λ_4} correspond respectively to the 2nd and 4th numerical scalar artificial dissipation fluxes. These have been added to the equation due to use of 2nd-order centered Jameson scheme (Jameson et al. [19]) in the numerical simulations. Therefore, the novel method allows the quantification of artificial dissipation fluxes on the balance of the axial momentum equation. Moreover, it is possible to localize regions and flow structures where these fluxes are active. Finally, notice that each term of Eqn. 7 is homogeneous to a force per unit volume ($[\mathrm{kg.m^{-2}.s^{-1}}]$).

Application of the ESA Model

On Steady Flows In the case of steady flow problems, time derivative terms are null leading to a balance of the advective and viscous fluxes and forces per volume unit. In practice, the precision of this equilibrium depends on the value of the numerical residual $\mathbf{R}$. For numerical data, it tends to reach zero at convergence according to the machines precision. Eqn. 3 can be simplified as follows:

$$\mathbf{R}(\mathbf{Q}) \approx 0 \iff \sum_{i=1}^{6} \mathbf{F} \cdot \mathbf{N}_{\Sigma_i} - V\,\mathbf{T}_{\Omega} \approx 0 \tag{8}$$

On Unsteady Flows Concerning unsteady flow problems, time derivative terms need to be determined since they can strongly impact the equilibrium of the equations. Those are taken equal to $-\mathbf{R}(\mathbf{Q})$, which is consistent only if the result analysed is a time consistent solution (usually a periodic solution).

The current approach can be applied both on unsteady and time-averaged solution allowing access of specific information of the numerical modelling residual. In fact, assuming that any flow variable $\mathbf{Q}$ can be decomposed into its mean term $\overline{\mathbf{Q}}$ plus its deterministic component $\mathbf{Q}'$ (stochastic component $\mathbf{Q}''$ is neglected), i.e. $\mathbf{Q} = \overline{\mathbf{Q}} + \mathbf{Q}'$, and by replacing each variable in the Eqn. 3, the residual operator can be written as:

$$\overline{\mathbf{R}(\mathbf{Q})} = \mathbf{R}\left(\overline{\mathbf{Q}}\right) + \overline{\mathbf{R}(\mathbf{Q}')} = 0 \tag{9}$$

where $\overline{\mathbf{R}(\mathbf{Q})}$ denotes the time-averaged balance of equation and tends to zero since the unsteady problem is periodic in time. $\mathbf{R}\left(\overline{\mathbf{Q}}\right)$ designates the residual applied to the time-averaged flow field. $\overline{\mathbf{R}(\mathbf{Q}')}$ indicates the time-averaged effect of the unsteadiness (also called Lumped Deterministic Source Terms by Ratzlaff et al. [20]).

INVESTIGATED COMPRESSOR

Description of the Test Compressor CREATE

The subsonic compressor used for the present work is the research multistage compressor dedicated to aero-thermal and aerodynamic studies. This $3\frac{1}{2}$-stage axial compressor named CREATE (Compresseur de Recherche pour l'Etude des effets Aérodynamiques et Technologiques, Fig. 1) has been designed by SNECMA and is tested at Ecole Centrale Lyon in LMFA Research laboratory. Its geometry and rotation speed are representative of High Pressure Compressor median-rear blocks of modern turbojet engine. Its design features are recalled in Tab. 1.

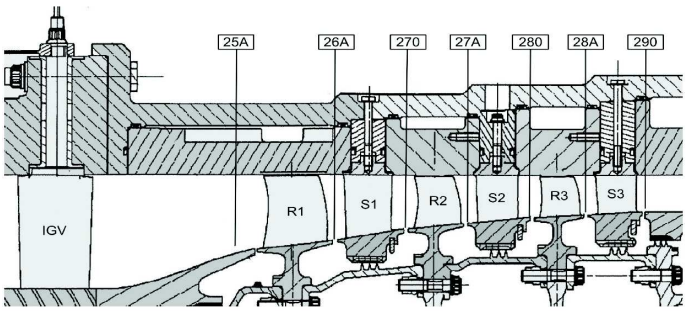

FIGURE 1. CROSS SECTION OF THE CREATE HIGH PRESSURE COMPRESSOR AND MEASUREMENTS PLANES.

Cylindrical outer casing diameter	0.52 m
Rotation speed	11543 rpm
Tip rotor speed	313 $\mathrm{m.s^{-1}}$

TABLE 1. DESIGN FEATURES OF CREATE.

Row	IGV	R1	S1	R2	S2	R3	S3
Number of blades per row (for 2π)	32	64	96	80	112	80	128
Number of blades for $2\pi/16$	2	4	6	5	7	5	8

TABLE 2. NUMBER OF BLADES OF CREATE ROWS.

CREATE's geometry was adapted in order to take into account technological constraints coming from the experimental part of the project. Thus, axial gaps were slightly increased compared to current compressors. The circumferential periodicity of the whole machine has been reduced to $2\pi/16$ choosing the number of blades of each rotor and stator as a multiple of 16 (Tab. 2). Consequently, measurements carried out over a sector of only $2\pi/16$ (namely 22.5°) contain all the spatial information in the case of stabilized operating points. The compressor and the inter-row measurement sections are presented in Fig.1. More details about the compressor design can be found in Touyeras and

Villain [21]. Notice that the compressor has a cylindrical casing. Thanks to the large amount of measurements, this experimental compressor has been the subject of different research works focused on rotor/stator interactions (Arnaud et al. [22, 23]) and CFD methods calibration and improvement (Sharma et al. [24], Marty et al. [25], Gourdain et al. [26]).

Design of the Casing Treatment

It was numerically seen at nominal speed that the stability of the untreated casing compressor is limited by the tip clearance effects on stages 2 and 3 (Gourdain et al. [26]). As a result, it was chosen to implement on both stages a CT in the form of five casing grooves of equal width and equally distributed in the axial direction. Details of the design study can be found in Perrot et al. [5]. Note that for confidentiality reasons, slots dimensions are not mentioned and the following results are normalized.

Experimental procedure

Experimental data have been obtained using both probes and Laser Doppler Anemometer (LDA) at constant radius locations in inter-row sections (Fig. 1). Modifications of the compressor casing at rotor R2 position have been done to provide sufficient optical access for the LDA measurements. Therefore, detailed unsteady flow measurements of the R2 near casing flow and in the CT grooves are available. A backskatter LDA designed and built by Dantec was used to perform measurements. Two pairs of beams measure simultaneously two velocity components (axial and tangential). The signals are treated by two Dantec real-time signal analyzers. Measurements are triggered with the compressor rotation frequency in such a way that the flow field is described either inside a single blade passage, or within several blade passages covering the circumferential periodicity of the whole machine. The data reduction process filters the random time scales of the turbulent flow. The unsteadiness captured only relates to phenomena clocked with the rotor passing frequency. The compressor was seeded with a polydisperse aerosol of paraffin oil. The mean size of particles at the outlet of the seeding generator was measured smaller than $1\mu m$. Seeding was performed upstream of the settling chamber. In such a flow configuration (low centrifugal forces and moderated decelerations), Ottavy et al. [27] proved that this technique was reliable. Once all the quantifiable uncertainties have been taken into account, the velocity component measurement error is about $\pm 1.5\%$. Details of the experimental instrumentations can be found in Arnaud et al. [22, 23].

DESCRIPTION OF THE NUMERICAL MODEL

To reduce the computational costs, it was chosen to restrict the investigation to the influence of upstream S1 stator wakes on R2. This choice is justified by the fact that R2 incoming flow is broadly the same for both SW and CT configurations whereas it differs at rotor R3 inlet due to R2 grooves impact. Therefore, in order to evaluate the only effect of the unsteadiness on the grooves, it is more judicious to analyse the configuration S1-R2.

Regarding the data base available, numerical predictions of overall performance are validated on the whole configuration R1-S3 using steady simulations carried out with the NS3D code *elsA*. Afterwards, unsteady simulations of the S1-R2 SW and CT configurations are performed and compared for further validation with experimental data. Steady simulations of the S1-R2 configurations are also conducted in order to evaluate difference between steady and unsteady approaches. Then, numerical results are analysed using the ESA model.

Numerical Procedure

Numerical simulations are carried out using the *elsA* software developed by ONERA and CERFACS (Cambier and Veuillot [28]). The code solves the Favre-Reynolds-averaged Navier-Stokes equations on multi-block structured meshes using a cell-centered finite-volume approach. It also allows the use of the Chimera method dedicated to complex geometries typically generated by technological effects (Castillon et al. [29]). Computations are run with a 2^{nd}-order centered Jameson scheme (Jameson et al. [19]) for the estimation of convective fluxes.

For steady flow computations, the time-marching is performed by using an efficient implicit time integration scheme, based on the backward Euler scheme and a scalar Lower-Upper (LU) Symmetric Successive Over-Relaxation (SSOR) method. The turbulent viscosity is computed with the two equation model of Launder-Sharma based on a $k-\varepsilon$ low-Reynolds formulation. The flow is assumed to be fully turbulent since the mean Reynolds number based on the blade chord is approximately 5.10^6.

Concerning the unsteady flow S1-R2 computations, the use of phase-lagged boundary conditions at the rows interfaces and on the periodic boundaries enables to consider only one single blade passage for each row (Erdos et al. [30], Gerolymos et al. [31]). The time-marching method is coupled with a second order Dual-Time-Stepping method (Jameson [32]) to obtain a time consistent solution (usually a periodic solution). The physical time step is chosen so that 300 iterations and 250 iterations are set to solve the blade passing frequency of the opposite row respectively in the stator and rotor frame of reference. To reach a converged state in the inner loop, 10 sub-iterations are imposed to ensure at least two orders of reduction for the residuals magnitude.

Inlet boundary conditions are based upon experimental measurements and the freestream turbulence intensity is set to 2%. To model the outlet duct, a throttle condition is coupled with a simplified radial equilibrium. For each configuration, stage throttling is modified by imposing a static pressure downstream the

last stator with respect to a reference level of static pressure.

Meshing Strategy

The flow domain is discretized with a low Reynolds multi-block approach using a "O-4H" meshing strategy. The typical dimensions of a blade passage mesh are 131, 65 and 85 points respectively in the axial, tangential and radial directions. The tip leakage region is discretized using a "O-H" grid toplogy with 25 points in the radial direction. In the present study, the meshes are clustered towards the solid boundaries in order to reach the resolution requirement of $y^+ \approx 1$ (the size of the first layer is approximatively 1μm). They prove to produce grid independant results in steady state simulations. For the SW case, this meshing strategy leads to a total nodes number of respectively 7.4 and 2.4 millions grid points for the R1-S3 and S1-R2 configurations. The CT configurations are based on the SW meshes at which "H" Chimera blocks modelling the casing grooves have been added (Fig. 2). The total grid points of respectively the R1-S3 and S1-R2 configurations are 8.1 and 2.8 millions.

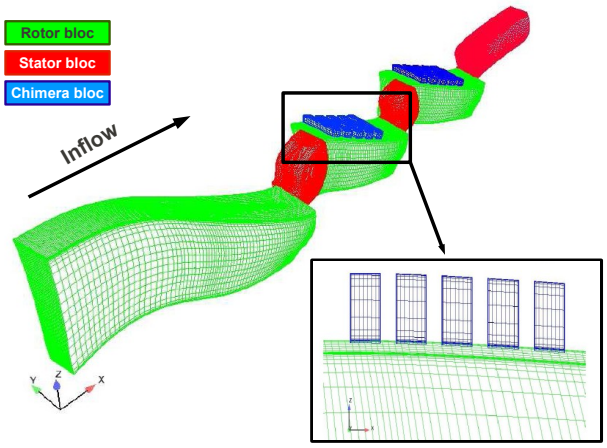

FIGURE 2. CHIMERA MESH USED FOR MODELLING THE CIRCUMFERENTIAL CASING GROOVES.

VALIDATION AND ASSESSMENT

Overall Performance on R1-S3 Configuration

Aerodynamic performances determined experimentally and by steady numerical calculations at nominal rotation speed for the R1-S3 SW and CT configurations are compared in Fig. 3. All data are normalized by the SW values at nominal operating conditions. Experimental uncertainties are 0.46%, 0.17% and 0.32% respectively for the mass flow rate, the pressure ratio and the isentropic efficiency. Concerning the steady numerical results, the limit of stability is estimated considering the last converged calculation.

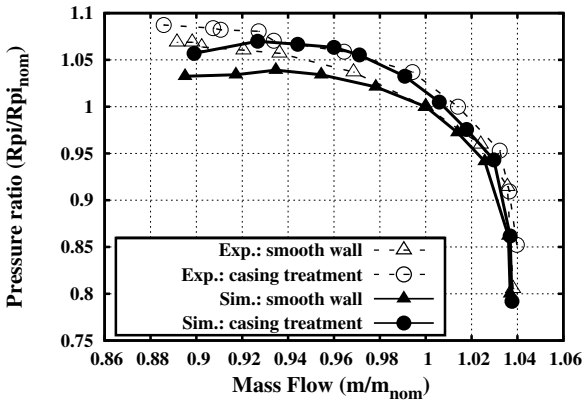

(a) PRESSURE RISE

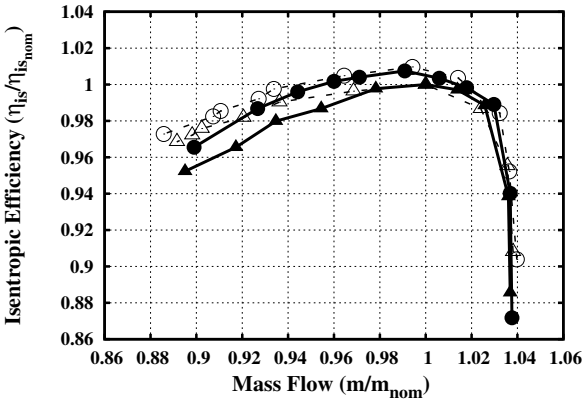

(b) ISENTROPIC EFFICIENCY

FIGURE 3. CREATE CHARACTERISTICS RELATIVE TO NOMINAL OPERATING POINT (EXPERIMENTAL VS. NUMERICAL SIMULATIONS).

Results in Fig. 3 show that the shapes of the pressure rise and isentropic efficiency curves are correctly represented by the simulations. The main information of Fig. 3 is that numerical simulation is able to predict the trend observed in the measurement that CT improves performances compared to the SW case. The relative shift in performance between both cases at design operating condition speed are approximately $\triangle\eta_{is,\max} = +1\%$, $\triangle Rpi_{\max} = +2\%$. The steady simulations of the whole compressor being validated, let us analyse the unsteady calculations of the S1-R2 configuration.

Unsteady Flow Details on S1-R2 Configuration

Phase-lagged unsteady simulations of S1-R2 SW and CT configurations are performed at the numerical design operating condition (i.e. $\dot{m}/\dot{m}_{\text{nom}} = 0.99$). This section compares the un-

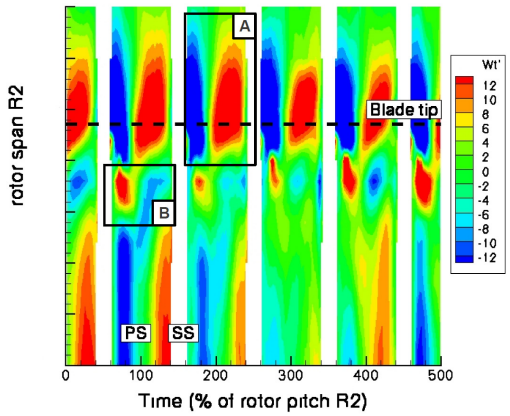

(a) LDA MEASUREMENT - $\dot{m}/\dot{m}_{\text{nom}} = 0.995$

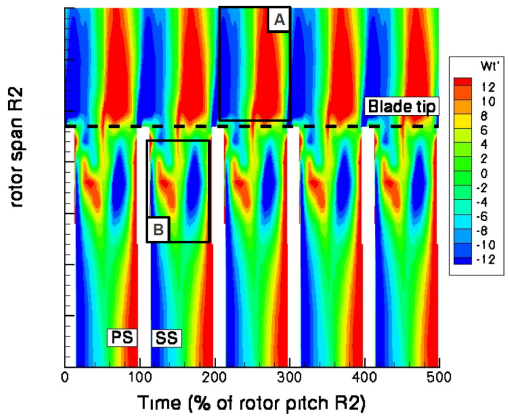

(b) SIMULATION - $\dot{m}/\dot{m}_{\text{nom}} = 0.99$

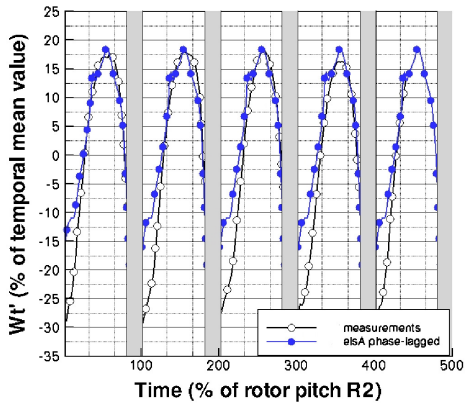

(c) COMPARISON AT h/H=100%

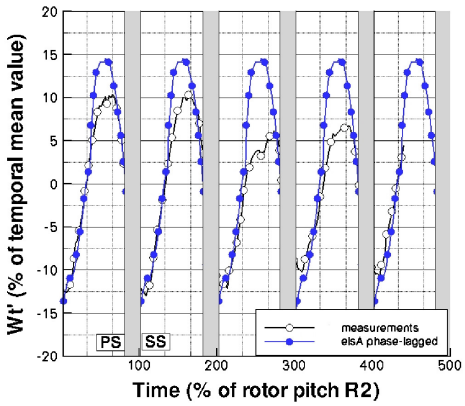

(d) COMPARISON AT MID-HEIGHT OF CT3 GROOVE

FIGURE 4. FLUCTUATION OF TANGENTIAL RELATIVE VELOCITY W'_θ AT FIXED AZIMUTHAL POSITION IN THE ABSOLUTE REFERENCE FRAME (EXPRESSED AS A RELATIVE PERCENTAGE OF THE TIME-RADIAL-AVERAGED VALUE $\overline{W_\theta}$).

steady LDA flow measurements and the numerical results in order to validate the unsteady approach. Notice that unsteady flow measurements were only available for the CT configuration.

Radial-time diagrams of tangential relative velocity fluctuations W'_θ are presented in Fig. 4 at the design operating point over a compressor time period $5T_{R2}$. These data are plotted for a fixed absolute angle position near mid-axial position in the CT3 groove. W'_θ is expressed as a percentage of the time-radial-averaged value $\overline{W_\theta}$. The white shaded bands denote shadow regions due to the blade and near blade rotor wall. Regarding results in Fig. 4(a) and 4(b), the unsteadiness of the tip rotor flow is well estimated by the simulations in terms of structures. Those results highlight two main regions of alternation of W'_θ respectively positive and negative characterizing the presence of vortex structures. The structure A observed in the CT3 groove is due to the R2 blade passage, whereas the structure B corresponds to the well-known tip leakage vortex. Based on these results, temporal evolutions at $h/H = 100\%$ (Fig. 4(c)) and at mid-CT3 height (Fig. 4(d)) of W'_θ are plotted to evaluate respectively these two structures. Results show a very good agreement in term of fluctuation magnitude, thus supporting the validation of the numerical simulations at design operating point. Moreover, these observations confirm the good accuracy of the information exchanges between the overlapped Chimera CT and the blade channel meshes. Objectives are now to provide further insight into the flow mechanisms of circumferential groove CT according to the ESA model.

FLOW MECHANISMS ANALYSIS WITH THE ESA MODEL

In order to get further insight into the influence of S1 stator wakes on the R2 grooves mechanisms, the following paragraphs investigate the balance of the axial momentum equation (Eqn. 7)

in the R2 blade tip flow field. Equation 7 is chosen since the pressure rise across the rotor can be explicitly derived from it.

Based on the previous S1-R2 unsteady simulations at the nominal operating point, instantaneous axial momentum balance obtained for 25 instants equally spread over one S1 blade passing temporal period T_{S1} are analysed. Both SW and CT cases are investigated. At the same time, balances computed from the related steady simulations are considered in order to compare steady and unsteady time-averaged budgets, and evaluate the availability of steady approach for grooves conception.

Definition of the control volume

The control volume surrounds the R2 blade tip flow field (see Fig. 5). It is circumferentially delimited by the rotor blade pitch, axially extended upstream and downstream of the rotor blade tip, and radially bounded between the 5^{th} and the 20^{th} grid layers in the tip clearance (total: 25). Therefore, the radial thickness of the control volume does not go to zero due to the Chimera technique in the grooved configuration. In fact, the two last radial layers attached to the casing are used for interpolation between grooves and the blade passage blocks. These are not taken into account in the control volume since they can mislead the Navier-Stokes equations equilibrium.

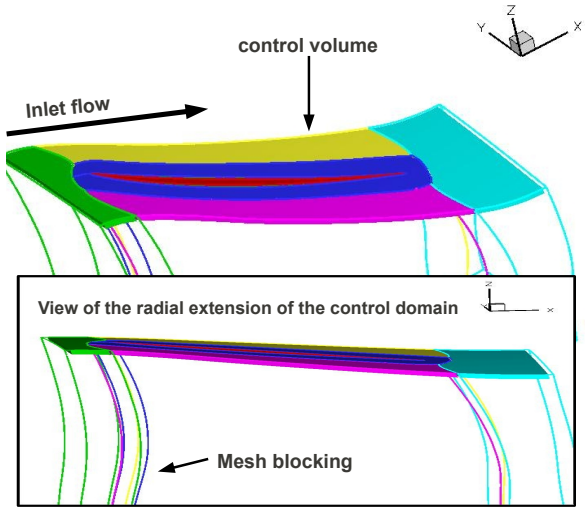

FIGURE 5. VIEWS OF THE CONTROL VOLUME IN THE ROTOR R2 TIP CLEARANCE USED FOR THE ANALYSIS.

Steady vs Time-Averaged Unsteady Global Flow Mechanisms

Results of the axial momentum balance for steady and unsteady phase-lagged of SW and CT configurations are shown as histograms in Fig. 6. This kind of representation provides a macroscopic view of the forces acting on the control volume Fig. 5. Note that the "phase-lagged results" correspond to the time-averaged balance over the compressor time period $6T_{S1}$ (i.e. $\overline{\mathbf{R}(\mathbf{Q})}$) of the instantaneous axial momentum balance (i.e. $\mathbf{R}(\mathbf{Q})$).

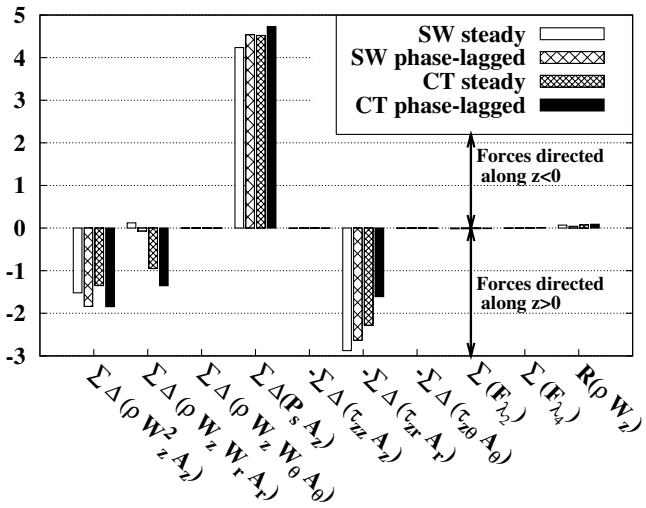

FIGURE 6. BUDGET ANALYSIS OF THE AXIAL MOMENTUM EQUATION FOR THE RESPECTIVE CONTROL VOLUMES OF THE SMOOTH AND GROOVED CASINGS.

Before discussing on the physical analysis, it is instructive to comment on the magnitude of the numerical terms of the steady and time-averaged unsteady balances. Steady results show that numerical modelling residual $\mathrm{R}(\rho W_z)$ tends to zero leading to a good precision of the balance of the equation. Similarly, the time-averaged temporal derivative term $(= -\overline{\mathrm{R}(\rho W_z)})$ obtained from unsteady simulations converges to zero. This observation lends support that the calculations correctly reach a time-periodic state. Moreover, it can be observed on both approaches that scalar artificial viscosity fluxes (F_{λ_2} and F_{λ_4}) are insignificant.

Steady and unsteady results of the SW configuration highlight the presence of three main terms that balance the steady axial momentum equation. Two different groups of forces can be distinguished. The first one is the class of forces that acts in opposite direction of the flow ($z < 0$), i.e. the adverse pressure force $\sum \triangle(P_s A_z)$ in this case. The second group includes the forces directed along the flow direction ($z > 0$) that balances the

previous force. It is composed of the net axial force due to the axial transport of the axial momentum $\sum\triangle(\rho W_z{}^2 A_z)$ and the net axial shear force on the radial faces of the control volume $-\sum\triangle(\tau_{rz}A_r)$ (induced by casing and blade tip boundary layers and tip leakage flow). All other terms are zero due to periodicity or to the cylindrical geometry of the control volume.

The grooves implementation has slightly increased the $\sum\triangle(P_sA_z)$ in agreement with the predicted overall performance in Fig. 3. As the SW case, the adverse pressure gradient remains the only force that opposes the advance of the main flow (Fig. 6). Due to flow exchanges between the grooves and the blade passage, CT is expected to contribute additionnal terms to balance this net axial pressure force. Based on results presented in Fig. 6, grooves contribute with radial transport of axial momentum $\sum\triangle(\rho W_zW_rA_r)$ as well as $-\sum\triangle(\tau_{rz}A_r)$ and $\sum\triangle(\rho W_z{}^2A_z)$ to balance $\sum\triangle(P_sA_z)$. It is interesting to note that the net axial force $\sum\triangle(\rho W_z{}^2A_z)$ is similar for both cases, suggesting that amplitude of W_z is independent of the presence of grooves in the configuration. Thereby, the change in magnitude of the term $\sum\triangle(\rho W_zW_rA_r)$ between SW and CT cases indicates that W_r acts as a "coefficient of amplification". In SW configuration, W_r at the casing vicinity and thus $\sum\triangle(\rho W_zW_rA_r)$ can be reasonably considered to be null or insignificant due to the cylindrical shape of the casing. In the opposite, CT grooves create some W_r at the casing due to fluid exchanges between the blade passage and the slots. Therefore, this phenomenon is expected to increase magnitude of the net axial force $\sum\triangle(\rho W_zW_rA_r)$. To respect the balance of the axial momentum equation, this increase is accompanied by a proportional decrease of the viscous effect $-\sum\triangle(\tau_{rz}A_r)$. This result can be expected since grooves remove surface that supports casing boundary layer and thus axial shear force. To resume, the main role of circumferential casing grooves is to create a radial velocity component W_r in the near casing flow region that generates $\sum\triangle(\rho W_zW_rA_r)$ in favor of a proportional reduction of the viscous effect. This effort is able to partially counteract the adverse pressure gradient and to enhance the performances in the region.

The comparison between steady and time-averaged unsteady results highlights one main discrepancy. It can be observed in Fig. 6 that the unsteady approach reduces the magnitude of axial shear force $-\sum\triangle(\tau_{rz}A_r)$ commensurate with an increase of the advective forces $\sum\triangle(\rho W_z^2A_z)$ and $\sum\triangle(\rho W_zW_rA_r)$. This trend is particularly pronounced over the CT results, thus providing evidence that groove mechanisms strongly depend on the unsteady flow features.

Unsteady Flow Mechanisms Figure 7 presents the temporal evolution of the main terms involved in the unsteady axial momentum balance. This kind of analysis allows us to gain a quantitative and qualitative knowledge of the contribution of the time derivative term $\partial\rho W_z/\partial t$.

Both SW and CT results show a sinusoidal time-dependent evolution of this term influenced by the stator S1 blade passage frequency T_{S1}. Its time-averaged value tends to zero, in agreement with results shown in Fig. 6. Concerning its temporal fluctuations, amplitudes are particularly pronounced for the CT case with higher values of a factor 2 compared to the SW.

Figure 8 presents results of a Fourier transform computed for the main time-dependent terms. Results show that time derivative amplitudes are mainly driven by those of $\sum\triangle(P_sA_z)$ in the SW case and those of $\sum\triangle(\rho W_zW_rA_r)$ in the CT case. In fact, CT deadens the magnitude of the $\sum\triangle(P_sA_z)$ fluctuations by a factor 2 which is believed to greatly enhance the flow stability (because the pressure gradient opposes the flow). The increase in $\sum\triangle(\rho W_zW_rA_r)$ fluctuation, which drives the time-dependent term, proves that groove mechanisms strongly responds to upstream flow unsteadiness.

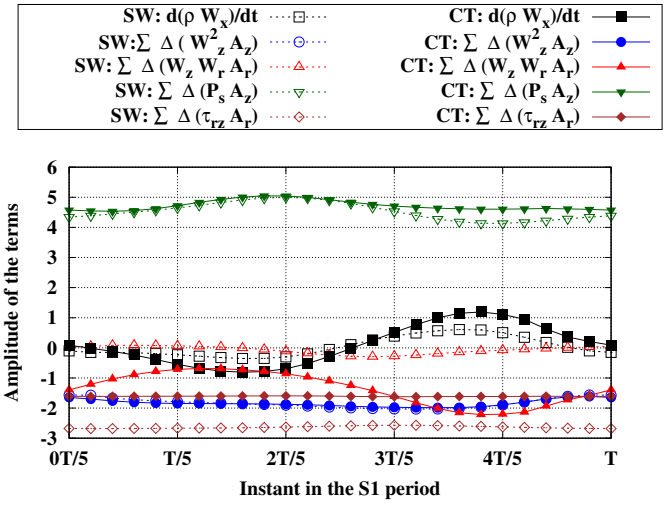

FIGURE 7. TEMPORAL EVOLUTION OF THE MAIN TERMS OF THE UNSTEADY AXIAL MOMENTUM EQUATION FOR THE SW AND CT CONTROL VOLUMES.

Individual Grooves Contribution The cumulative sum along the axial direction of the main terms of the axial momentum equation is presented in Fig. 9. Results are plotted for steady and time-averaged unsteady simulations of SW and CT configurations. These diagrams provide information on the region where flow is highly constrained and also individual grooves contribution. The shaded bands denote the axial location of the casing grooves.

Figure 9 shows similar curves shape of time-averaged adverse pressure gradient $\sum\triangle(P_sA_z)$ suggesting that the presence of CT grooves as well as the numerical approach steady/unsteady

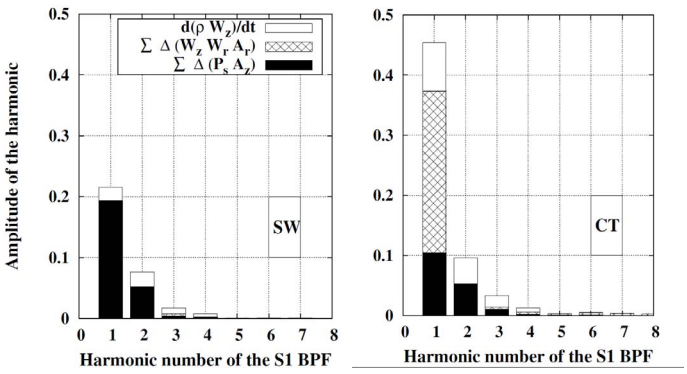

(a) SMOOTH WALL (b) CASING TREATMENT

FIGURE 8. FOURIER TRANSFORM OF THE MAIN TERMS OF THE UNSTEADY AXIAL MOMENTUM BALANCE SEEN FIG. 7.

have almost insignificant impact on the pressure rise from a time-averaged point of view. Concerning the term $-\sum\triangle(\tau_{rz}A_r)$, curves present the same global shape. However, results show that CT delays further downstream the origin of the shear force rapid growth occuring between the 2nd and the 3rd grooves in the SW case. This information is significant since this term, linked to velocity gradient, can be associated to a casing boundary layer thickening, i.e. a presence of aerodynamic blockage. Moreover, it is worth noticing that the axial shear force increases in magnitude commensurate with the increase of pressure rise across the rotor. As a result, the observation suggests that CT is able to slow down the rapid growth of flow blockage.

The main differences between SW and CT occur for the curves of net axial convective forces. Results of $\sum\triangle(\rho W_z W_r A_r)$ in Fig. 9, which are mainly opposed to the main flow direction ($\sum\triangle(\rho W_z W_r A_r) > 0$), show no difference until the trailing edge of the 3rd groove. This trend indicates that the first two grooves have no impact on the near casing flow. At this particular position, corresponding to the origin of the shear force rapid growth in the CT cases, CT curves diverge from the SW ones. In fact, the 3rd groove roughly changes the cumulative sum $\sum\triangle(\rho W_z W_r A_r)$ to negative value so that the axial force is turned in the same direction than the main flow, which thus is benefit to the stabilization effort. Further downstream, CT curves evolves similarly as the SW ones. Therefore, the last two grooves are believed to be no longer useful to the stabilization effort. This hypothesis is confirmed by suppressing the two last grooves at nominal operating point (see axial evolution of the term $\sum\triangle(\rho W_z W_r A_r)$ in Fig. 10). Concerning the term $\sum\triangle(\rho W_z^2 A_z)$ in Fig. 9, curves mainly evolve in opposite magnitude than $\sum\triangle(\rho W_z W_r A_r)$. This observation lends support that the radial velocity component W_r is of a main interest for the stability of the tip flow.

The change in axial momentum balance between steady and unsteady approaches can be assessed with the help of Fig. 9. SW

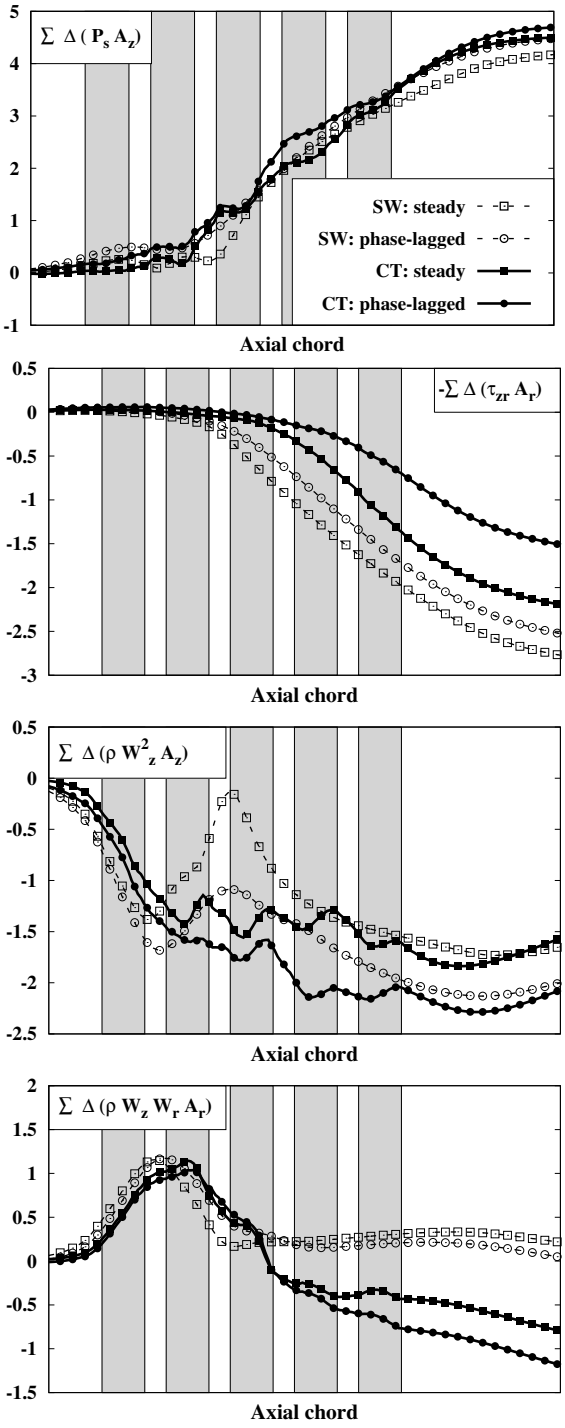

FIGURE 9. CROSS COMPARISONS STEADY/UNSTEADY AND SW/CT OF THE EVOLUTION OF THE CUMULATIVE SUM IN THE AXIAL DIRECTION OF THE MAIN TERMS OF THE AXIAL MOMENTUM EQUATION.

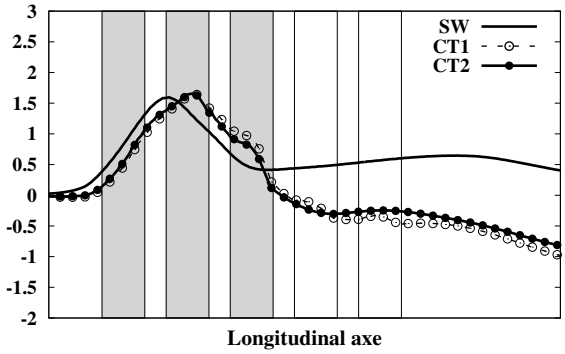

FIGURE 10. COMPARISONS BETWEEN SW, CT1 (5 GROOVES) AND CT2 (3 GROOVES) OF THE EVOLUTION OF THE CUMULATIVE SUM IN THE AXIAL DIRECTION OF $\sum\triangle(\rho W_z W_r A_r)$.

and CT curves show that unsteady simulations predict higher magnitude of $\sum\triangle(\rho W_z^2 A_z)$ in the 2^{nd} groove neighbourhood. This result suggests that the blockage effect induced by the tip leakage flow is more pronounced in the unsteady approach. The reason comes from the interaction between the upstream stator wakes and the tip leakage flow. The effect of the increased blockage also affects the other terms in order to respect the balance of the axial forces.

The other main observation concerns the CT mechanisms. While steady and unsteady CT plots of $\sum\triangle(\rho W_z W_r A_r)$ in Fig. 9 reveal no difference for the three first grooves mechanisms, unsteady curves show an increase in magnitude at the beginning of the two last grooves. Both increase is associated with a decrease in axial shear force $-\sum\triangle(\tau_{rz} A_r)$, which could enhance the overall performance. It was shown in Fig. 7 and 8 that in the CT case the unsteadiness was driven by the temporal fluctuations of W_r which stabilizes the compression system. It is shown in Fig. 9 that the time-averaged effect of the W_r fluctuations is effective in the two last grooves. This remark is all the more important that the two rear grooves has shown to be inefficient in a steady point of view. As a result, implementation of circumferential groove mechanisms in a multistage compressor has to be studied using unsteady simulations.

CONCLUSION

This paper has presented a generalized method of the Shabbir and Adamczyk approach for uncovering the flow mechanisms induced by CT using CFD numerical simulations. Compared to Shabbir's approach, this method allows analysis of any CT geometry thanks to a budget analysis of the Navier-Stokes unsteady momentum equations. In the paper, only the unsteady steady axial momentum equation is analysed.

The ESA method has been used to investigate the influence of upstream stator wakes on circumferential casing grooves mechanisms. Therefore, an experimental multistage subsonic compressor representative of those implemented in modern engines has been numerically investigated. Unsteady simulations have been performed and validated with LDA experimental data. Based on these numerical results, the method reveals that the radial velocity component W_r is the key to the gain in the near casing flow stabilization. Thanks to radial flow exchange between slots and compressor through-flow stream, circumferential CT are able to bring substantial effort to balance the adverse pressure gradient through an increase of the net axial force due to radial transport of axial momentum $\sum\triangle(\rho W_z W_r A_r)$. Moreover, the pressure gradient temporal fluctuation responsible for unsteadiness in the SW configuration has been deaden by the CT thanks to the temporal fluctuation of W_r. It is thus shown that axisymmetric CT stabilizes the compression system all the more the inlet conditions are time-dependant.

The ESA method also shows its capability to assess grooves effectiveness.

A perspective of this work will be to assess the axisymmetric CT effect over the complete operating range. Other points of interest will be the study of non-axisymmetric CT in order to evaluate the contribution of the pressure fluctuation to the compression stability.

ACKNOWLEDGMENT

The authors are grateful to Snecma, SAFRAN Group, for permission to publish results. Special thanks to LMFA and CERFACS-CFD Team for their computational facilities as well as for their availability for discussions concerning numerical methods and physical analysis. The authors are also grateful to the *elsA* software team (ONERA).

REFERENCES

[1] Greitzer, E. M., Nikkanen, J. P., Haddad, D. E., Mazzawy, R. S., and Joslyn, H. D., 1979. "A fundamental criterion for the application of rotor casing treatment". *J. of Fluids Engineering,* ***101***(3), pp. 237–243.

[2] Hathaway, M. D., 2007. *Passive Endwall Treatments for Enhancing Stability*. VKI LS 2006-06 on Advances in Axial Compressor Aerodynamics.

[3] Rabe, D., and Hah, C., 2002. "Application of casing circumferential grooves for improved stall margin in a transonic axial compressor". In proceedings of ASME Turbo Expo 2002, paper GT2002-30641.

[4] Shabbir, A., and Adamczyk, J. J., 2005. "Flow mechanism for stall margin improvement due to circumferential casing

grooves on axial compressors". *ASME J. of Turbomachinery,* ***127***(4), pp. 708–718.

[5] Perrot, V., Touyeras, A., and Lucien, G., 2007. "Detailed cfd analysis of a grooved casing treatment on an axial subsonic compressor". In proceedings of 7th European Turbomachinery Conference.

[6] Müller, M. W., Schiffer, H.-P., and Hah, C., 2007. "Effect of circumferential grooves on the aerodynamic performance of an axial single-stage transonic compressor". In proceedings of ASME Turbo Expo 2007, paper GT2007-27365.

[7] Müller, M. W., Biela, C., Schiffer, H.-P., and Hah, C., 2008. "Interaction of rotor and casing treatment flow in an axial single-stage transonic compressor with circumferential grooves". In proceedings of ASME Turbo Expo 2008, paper GT2008-50135.

[8] Houghton, T., and Day, I. J., 2009. "Enhancing the stability of subsonic compressors using casing grooves". In proceedings of ASME Turbo Expo 2009, paper GT2009-59210.

[9] Legras, G., Gourdain, N., and Trebinjac, I., 2010. "Numerical analysis of the tip leakage flow field in a transonic axial compressor with circumferential casing treatment.". *J. of Thermal Science,* ***19***(3), pp. 198–205.

[10] Legras, G., Gourdain, N., and Trébinjac, I., 2011. "Extended methodology for analysing the flow mechanisms induced by casing treatment in compressor". In proceedings of 9th of European Turbomachinery Conference.

[11] Wilke, I., and Kau, H.-P., 2004. "A numerical investigation of the flow mechanisms in a high pressure compressor front stage with axial slots". *ASME J. of Turbomachinery,* ***126***(3), pp. 339–349.

[12] Wilke, I., Kau, H.-P., and Brignole, G., 2005. "Numerically aided design of a high-efficient casing treatment for a transonic compessor". In proceedings of ASME Turbo Expo 2005, paper GT2005-68993.

[13] Gourdain, N., and Leboeuf, F., 2009. "Unsteady simulation of an axial compressor stage with casing and blade passive treatments". *ASME J. of Turbomachinery,* ***131***(2), p. 021013.

[14] Vogues, M., Schnell, R., Willert, C., Mönig, R., Müller, M. W., and Zscherp, C., 2011. "Investigation of blade tip interaction with casing treatment in a transonic compressor - part 1: Particle image velocimetry". *ASME J. of Turbomachinery,* ***133***(1), p. 011007.

[15] Schnell, R., Vogues, M., Mönig, R., Müller, M. W., and Zscherp, C., 2011. "Investigation of blade tip interaction with casing treatment in a transonic compressor - part 2: Numerical results". *ASME J. of Turbomachinery,* ***133***(1), p. 011008.

[16] Hathaway, M. D., 2002. "Self-recirculating casing treatment concept for enhanced compressor performance". In proceedings of ASME Turbo Expo 2002, paper GT-2002-30368.

[17] Yang, H., Nuernberger, D., Nicke, E., and A., W., 2003. "Numerical Investigation of Casing Treatment Mechanisms with a Conservative Mixed-Cell Approach". In proceedings of ASME Turbo Expo 2003, paper GT2003-38483.

[18] Strazisar, A. J., Bright, M. J., Thorp, S., Culley, D. E., and Suder, K. L., 2004. "Compressor stall control through endwall recirculation". In proceedings of ASME Turbo Expo 2004, paper GT2004-54295.

[19] Jameson, A., Schmidt, R. F., and Turkel, E., 1981. Numerical Solutions of the Euler Equations by Finite Volume Methods Using Runge-Kutta Time Stepping. AIAA paper AIAA-81-1259.

[20] Ratzlaff, J., Orkwis, P. D., Noll, C., and Steuber, G., 2008. "Analysis of lumped deterministic source terms and their sub-components in a stage 1 high pressure turbine rotor". In proceedings of ASME Turbo Expo 2008, paper GT2008-51473.

[21] Touyeras, A., and Villain, M., 2004. "Aerodynamic design and test result analysis of a three stage research compressor". In proceedings of ASME Turbo Expo 2004, paper GT2004-53940.

[22] Arnaud, D., Ottavy, X., and Vouillarmet, A., 2004. "Experimental investigation of the rotor-stator interactions within a high-speed, multi-stage, axial compressor. part 1 - experimental facilities and results". In proceedings of ASME Turbo Expo 2004, paper GT2004-53764.

[23] Arnaud, D., Ottavy, X., and Vouillarmet, A., 2004. "Experimental investigation of the rotor-stator interactions within a high-speed, multi-stage, axial compressor. part 2- modal analysis of the interactions". In proceedings of ASME Turbo Expo 2004, paper GT2004-53778.

[24] Sharma, V., Schvallinger, M., Marty, J., Gaible, H., Legras, G., Aupoix, B., and Houdeville, R., 2007. "Turbulence modelling effects on off-design predictions for a multistage compressor". In proceedings of 18th ISABE, paper 2007-1183.

[25] Marty, J., Cottin, G., and Aupoix, B., 2009. "Turbulence modelling and transition to turbulence effects for a high pressure multistage compression". In proceedings of 8th European Turbomachinery Conference.

[26] Gourdain, N., Ottavy, X., and Vouillarmet, A., 2009. "Experimental and numerical investigation of unsteady flows in a high speed three stages compressor". In proceedings of 8th European Turbomachinery Conference.

[27] Ottavy, X., Trébinjac, I., and A., V., 2001. "Analysis of the interrow flow field within a transonic axial compressor: Part 1- experimental investigation". *ASME J. of Turbomachinery,* ***123***(1), pp. pp. 49–56.

[28] Cambier, L., and Veuillot, J.-P., 2008. "Status of the elsa software for flow simulation and multidisciplinary applica-

tions". In proceedings of 46th AIAA Aerospace Science Meeting and Exhibit, paper 2008-664.
[29] Castillon, L., Péron, S., and Benoit, C., 2010. "Numerical simulations of technological effects encountered on turbomchinery configurations with the chimera technique". In proceedings of 27th ICAS, paper 088.
[30] Erdos, J. I., Alznert, E., and McNally, W., 1977. "Numerical solution of periodic transonic flow through a fan stage". *AIAA Journal,* ***15***(11), pp. 1559–1568.
[31] Gerolymos, G. A., Michon, G. J., and Neubauer, J., 2002. "Analysis and application of chorochronic periodicity in turbomachinery rotor/stator interaction computations". *J. of Propulsion and Power,* ***18***(6), pp. 1139–1152.
[32] Jameson, A., 1991. "Time dependent calculations using multigrid, with applications to unsteady flows past airfoils and wings". In proceedings of 10th AIAA Computational Fluid Dynamics Conference, paper 91-1596.